

REArtGS: Reconstructing and Generating Articulated Objects via 3D Gaussian Splatting with Geometric and Motion Constraints

Di Wu^{1,2}, Liu Liu^{3,*}, Zhou Linli¹, Anran Huang³, Liangtu Song¹, Qiaojun Yu⁴, Qi Wu^{4,5}, Cewu Lu⁴

¹ Hefei Institutes of Physical Science Chinese Academy of Sciences

² University of Science and Technology of China

³ Hefei University of Technology

⁴ Shanghai Jiao Tong University

⁵ ByteDance

* Corresponding Author, Email: liuliu@hfut.edu.cn

Abstract

Articulated objects, as prevalent entities in human life, their 3D representations play crucial roles across various applications. However, achieving both high-fidelity textured surface reconstruction and dynamic generation for articulated objects remains challenging for existing methods. In this paper, we present REArtGS, a novel framework that introduces additional geometric and motion constraints to 3D Gaussian primitives, enabling high-quality textured surface reconstruction and generation for articulated objects. Specifically, given multi-view RGB images of arbitrary two states of articulated objects, we first introduce an unbiased Signed Distance Field (SDF) guidance to regularize Gaussian opacity fields, enhancing geometry constraints and improving surface reconstruction quality. Then we establish deformable fields for 3D Gaussians constrained by the kinematic structures of articulated objects, achieving unsupervised generation of surface meshes in unseen states. Extensive experiments on both synthetic and real datasets demonstrate our approach achieves high-quality textured surface reconstruction for given states, and enables high-fidelity surface generation for unseen states. Codes will be released after acceptance and the project website is at <https://sites.google.com/view/reartgs/home>.

1. Introduction

Articulated objects are ubiquitous in our daily lives. Modeling articulated objects, i.e. mesh reconstruction and generation, holds significant importance in many fields of computer vision and robotics fields including virtual and augmented reality [17, 33], object manipulation [29, 37] and human-object interaction [13, 34]. Currently, the surface and shape reconstruction for articulated objects is a non-trivial task due to the challenges: firstly, articulated objects

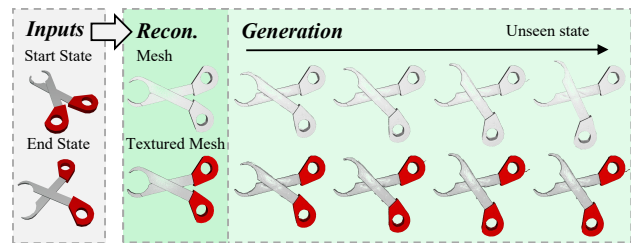


Figure 1. Given multi-view RGB images of articulated objects from two arbitrary states, our REArtGS enables high-quality textured surface mesh reconstruction and generation for unseen states.

exhibit complicated and diverse geometric structures with a wide range of scales. Secondly, articulated objects possess varied kinematic structures, and the static surface meshes generated from vanilla 3D reconstruction methods fail to meet practical interaction requirements.

Under this circumstance, PARIS [15] attempts using multi-view images from two states to dynamically reconstruct articulated objects with neural implicit radiance fields. Nevertheless, we make observation that PARIS holds two problems leading to difficulty in reconstructing high-quality surface meshes: (1) It relies on neural implicit representation to reconstruct objects, lacking constraints on geometric learning, which leads to shape-radiance ambiguity and additional errors when extracting surface meshes from the learned entangled neural representations. (2) PARIS fails to generate texture-rich meshes for articulated objects, while texture is significant for bridging sim-to-real gap.

In recent years, 3D Gaussian Splatting (3DGS) [11] achieves realistic and real-time novel view synthesis through explicit representation with 3D Gaussian primitives. Some subsequent works have expanded 3DGS to surface reconstruction [1, 7, 39] and dynamic reconstruction

[4, 14, 35]. However, existing 3DGS-based surface reconstruction methods typically suffer from insufficient geometric constraints [39] or impose constraints by restricting the shapes of Gaussian primitives [6, 7], leading to artifacts or inaccurate recovery of detail structures. On the other hand, current dynamic reconstruction methods via 3DGS tend to input motion time and spatial positions into neural networks to obtain the deformed positions of Gaussian primitives [4, 35]. Consequently, these methods require continuous supervision throughout the entire motion, which limits their ability to generate surface meshes in unseen states. In general, introducing 3DGS as a ready-to-use technique into articulated object surface reconstruction and generation is still not feasible and remains a challenging task.

In this paper, to address the aforementioned issues and make full advantage of 3DGS, we propose **REArtGS**, a novel approach that **R**econstructs and **g**enerates high-quality texture-rich mesh surfaces for **A**rticulated objects via 3D Gaussian Splatting, only taking multi-view RGB images from two arbitrary states. We firstly introduce an unbiased Signed Distance Function (SDF) guidance to regularize Gaussian opacity fields, enhancing geometry constraints and improving surface reconstruction quality. Then we employ the optimized Gaussian primitives as an accurate geometry initialization for dynamic surface generation. In addition, we leverage the kinematic structures of articulated objects to model time-continuous Gaussian deformable fields in an unsupervised fashion. Our REArtGS is evaluated on PartNet-Mobility [31] and AKB-48 [16] object repositories, ranging from synthetic to real-world data. Extensive experiments demonstrate that our REArtGS outperforms existing state-of-the-art methods in articulated object surface reconstruction and generation tasks.

In summary, our main contributions can be summarized as follows: (1) We propose REArtGS, a novel framework introducing 3DGS to conduct high-quality textured surface reconstruction and time-continuous generation for articulated objects, only using multi-view images from two arbitrary states. (2) Our REArtGS exploits an unbiased SDF guidance for 3D Gaussian primitives to enhance geometric constraints for improving reconstruction quality, and also establishes the deformable fields constrained by kinematic structures of articulated objects to generate unseen states in an unsupervised manner. (3) We incorporate REArtGS into various scenes ranging from synthetic to the real-world data across many different articulation categories. The extensive experimental results demonstrate that our approach significantly outperforms SOTAs in both mesh reconstruction and generation tasks.

2. Related Work

2.1. Articulated Object Shape Reconstruction

Object surface reconstruction is a well-established problem for understanding the full geometric shape of objects. Some works introduce to encode continuous functions that model the objects using Signed Distance [23], radiance [20, 26, 28] and occupancy [19]. Going beyond static scenes with rigid objects, A-SDF [21] extends the DeepSDF to learn a latent code for modeling an articulated object by both shape and motion. Following up on A-SDF, CenterSnap [8] designs a point cloud decoder for shape reconstruction, and Shapo [9] fully utilizes shape prior for latent space learning. To generalize these works into the real world, AKB-Net [16] integrates the shape reconstruction module into the object knowledge modeling along with part segmentation and pose estimation. To achieve both geometry and motion analysis in a single forward, Ditto [10] and REACTO [27] propose to generate shapes at unseen states from pair observations. Currently, PARIS [15] alleviate the 3D data requirement limitation and success to reconstruct shape surface with only RGB images. But it still suffer from several challenges such as lacking constraints modeling and failing in texture generation. Therefore, our REArtGS aims to address these issues, and proposes geometric and motion constrained 3DGS for this task.

2.2. Surface Reconstruction with 3DGS

3D Gaussian Splatting has become increasingly popular technique for surface reconstruction in recent years [11, 12, 25, 38]. GOF [39] establishes opacity fields of 3D Gaussians using ray-tracing-based rendering, and extracts the surface meshes by the opacity level set. 2DGS [7] and PGSR [1] seek to transform 3D Gaussians into 2D flat representation, obtaining accurate normal distribution. Although improving the surface reconstruction quality, these methods still lack more reasonable geometry constraints. Several researchers attempt to integrate SDF representation with 3D Gaussians [2, 3, 32, 36], but these approaches commonly use SDF to regularize normals and guide the pruning of 3D Gaussians, without substantial optimization of Gaussian opacity fields. Meanwhile, some works conduct dynamic reconstruction using 3DGS. Deformable 3DGS proposes a deformation field to reconstruct dynamic scenes with 3D Gaussian primitives. 4DGS [4] leverages a spatial-temporal structure encoder and a multi-head Gaussian deformation decoder to derive the deformed 3D Gaussians at a given time. However, these methods rely on complete supervision of the motion process, limiting their capacity for generating unseen states. The similar issues also occur in DGMesh [14] and REACTO [27]. Additionally, these methods lack an adequate initialization for the canonical geometry, leading to a decline in surface quality when directly

conducting dynamic rendering.

3. Method

The overall framework of our REArtGS is illustrated in Fig. 2. Taking multi-view RGB images from two arbitrary states $s = 0, s = 1$ of articulated objects, we aim to achieve high-quality textured mesh reconstruction and generation at any unseen states between $s \in [0, 1]$.

We first introduce SDF representation and propose an unbiased SDF regularization to enhance the geometry constraints of 3D Gaussian primitives. In this manner, we improve the reconstruction quality and yield dense point clouds at state $s = 0$, providing an accurate geometric prior for subsequent dynamic reconstruction. Then we establish time-continuous deformable fields for 3D Gaussian primitives constrained by the kinematic structures of articulated objects. Given any state s , we can derive the deformed position x_s of Gaussian primitives through the deformation fields in an unsupervised fashion. The details of our approach are elaborated below.

3.1. Reconstruction with Unbiased SDF Guidance

To better preserve the geometric features of Gaussian primitives, we use the ray-tracing-based 3DGS following GOF, which evaluates rendering contribution of Gaussian primitives directly without the 3D-to-2D projection step. However, the Gaussian primitives still suffer from insufficient geometric constraints. Concretely, the opacity fields lack an explicit link with scene surface, which may lead to noisy outputs in surface reconstruction of articulated objects.

To address the limitation, we first introduce SDF representation to guide the geometry learning of Gaussian primitives. We utilize a Multi-layer Perceptrons (MLP) with 8 hidden layers to learn the SDF values for spatial position inputs, and the scene surface can be represented by the zero-set:

$$\mathcal{S} = \{\mathbf{x} \in \mathbb{R}^3 \mid f(\mathbf{x}) = 0\} \quad (1)$$

Following Neus [30], we can derive the opacity $\hat{\sigma}$ for the center \mathbf{x}_i of Gaussian G_i from learned SDF values:

$$\hat{\sigma}_i = \max\left(\frac{\Phi(f(\mathbf{x}_i)) - \Phi(f(\mathbf{x}_{i+1}))}{\Phi(f(\mathbf{x}_i))}, 0\right) \quad (2)$$

where Φ denotes a Sigmoid function. Nevertheless, the SDF-opacity conversion is not directly applicable to the α blending rendering. This is because each 3D Gaussian primitive models a local density distribution, while Eq. 2 only maps the global positions to their opacity values and neglects the local properties of Gaussian primitives. Therefore, we define the opacity of Gaussian primitive combining

the rendering contribution ε proposed in GOF as:

$$\begin{aligned} \sigma_i &= \hat{\sigma}_i \varepsilon(G_i) \\ &= \hat{\sigma}_i \cdot \max(e^{-\frac{1}{2}\mathbf{x}_L^T \mathbf{x}_L}) \\ &= \hat{\sigma}_i \cdot \max\left(e^{-\frac{1}{2}(\mathbf{r}_L^T \mathbf{r}_L t^2 + 2\mathbf{o}_L^T \mathbf{r}_L t + \mathbf{o}_L^T \mathbf{o}_L)}\right) \end{aligned} \quad (3)$$

where $\mathbf{o}_L, \mathbf{r}_L$ are the camera center and incident ray direction represented in the local coordinate system of Gaussian G_i , which can be acquired by local scaling matrix and rotation matrix of G_i . The maximum value of $\varepsilon(G_i)$ occurs at ray depth t^* , expressed as follows:

$$t^* = \frac{\mathbf{o}_L^T \mathbf{r}_L}{\mathbf{r}_L^T \mathbf{r}_L} \quad (4)$$

The rendering equation based on σ is represented as:

$$\mathbf{C} = \sum_{i=1}^N \mathbf{c}_i \sigma_i \prod_{j=1}^{i-1} (1 - \sigma_j) \quad (5)$$

where N is the number of Gaussian primitives involved in α -blending and \mathbf{c}_i is the color modeled with spherical harmonics. To leverage SDF to constrain the geometric learning of Gaussian primitives, we first introduce a bell-shaped function Φ_k to modulate the transformation from SDF to opacity and replace the original Sigmoid activation function Φ in Eq. 2, formulated as:

$$\Phi_k(f(\mathbf{x})) = \frac{e^{k \cdot f(\mathbf{x})}}{(1 + e^{k \cdot f(\mathbf{x})})^2} \quad (6)$$

where k is a learnable parameter that adjusts the function shape and we initially set it to 0.1. Intuitively, the Gaussian primitive closer to the surface has a higher opacity value.

However, since $\hat{\sigma}$ is determined solely by the Gaussian's center, a non-alignment still exists between the maximum points of $\hat{\sigma}$ and ε , which can be formulated as:

$$t_{bias} = \left\| \underset{t}{\operatorname{argmax}}(\hat{\sigma}) - \underset{t}{\operatorname{argmax}}(\varepsilon) \right\| \quad (7)$$

To mitigate this bias, we propose an unbiased regularization for the SDF value at depth t^* as following:

$$\mathcal{L}_{unbias} = \|f(\mathbf{o} + t^* \mathbf{r})\|_2^2 \quad (8)$$

where \mathbf{o}, \mathbf{r} are the camera center and incident ray direction. Through the unbiased regularization, we encourage that when the rendering contribution of a Gaussian primitive reaches its maximum value, the corresponding spatial position is close to the scene surface, as shown in Fig. 3. In this manner, the SDF representation is able to regularize the opacity fields without bias and facilitate more reasonable distribution of Gaussian primitives over scene surface. We provide more detailed elaboration and proof in the supplementary materials.

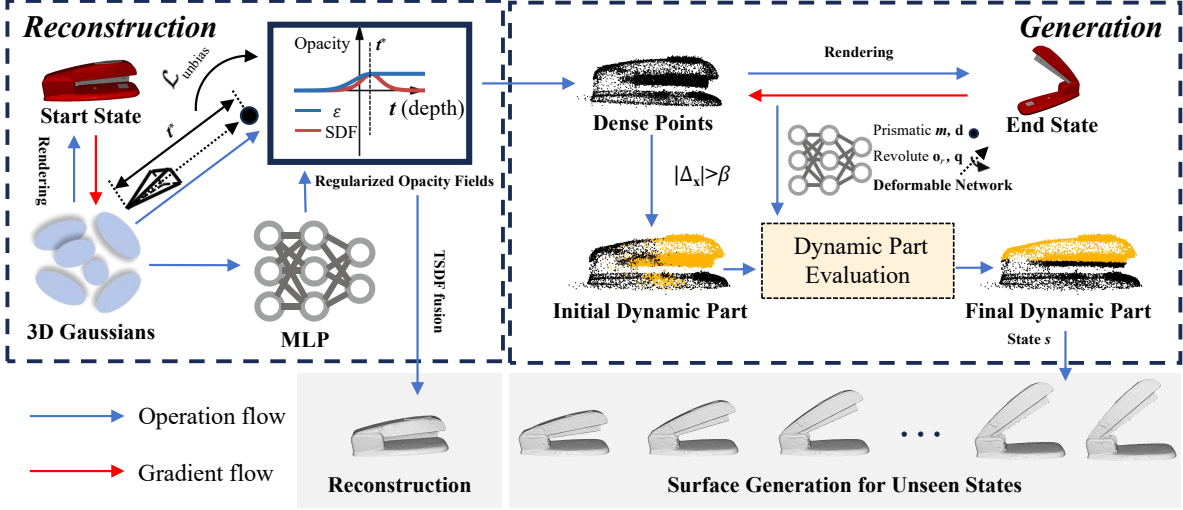


Figure 2. The overall pipeline of REArtGS. We introduce additional geometric and motion constraints for 3D Gaussian primitives, achieving high-quality surface mesh reconstruction and time-continuous generation, with only multi-view images from arbitrary two states.

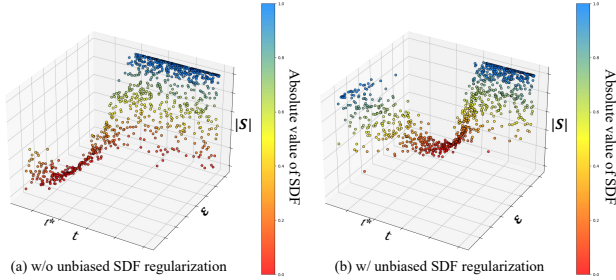


Figure 3. The illustration of unbiased SDF regularization. It can be observed that when t approaches t^* , the absolute value of SDF $|S|$ converges to zero with the unbiased SDF regularization.

3.2. Mesh Generation with Motion Constraints

Due to the explicit representation of Gaussian primitives, we can acquire accurate dense point clouds from reconstruction, serving as initial geometry for mesh generation. Then we establish time-continuous deformable fields for 3D Gaussians to infer the deformed position \mathbf{x}_s at state s . However, it is challenging to optimize the deformable fields for Gaussian primitives only with the supervision of two states. Accordingly, we exploit the kinematic structures of articulated objects to constrain the Gaussian deformation field. We first assume that the articulated motion only includes rotation and translation following PARIS. For a rotation joint, our learning objective is to determine its rotation axis and rotation angle. Specifically, we take the pivot point $\mathbf{o}_r \in \mathbb{R}^3$ of the rotation axis and a normalized quaternion $\mathbf{q} \in \mathbb{R}^4$ as learnable parameters, where the quaternion can be decoupled into the rotation axis $\mathbf{a} \in \mathbb{R}^3$ and rotation angle θ . For a prismatic joint, our learning objective is to determine their translation directions and translation distances. Similarly, we take the unit vector $\mathbf{d} \in \mathbb{R}^3$ representing the translation

direction and the translation distance m as learnable parameters.

Subsequently, we formulate the deformable fields through a canonical state. Given the rotation motion $SO(3) \in \mathbb{R}^{3 \times 3}$, we define its canonical state as $s^* = 0.5$ and the rotation angle of state s can be expressed as:

$$\theta_s = \frac{(s^* - s)\theta}{s^*} \quad (9)$$

where $s \in [0, 1]$ and $\theta \in [-\pi/2, \pi/2]$. The angle-bounded parameterization is able to prevent the singularity in exponential coordinates when $\|\theta\| > \pi$. Using Rodrigues' rotation formula [24], the deformed position \mathbf{x}_s can be derived as following:

$$\mathbf{x}_s = (\mathbf{I} + \sin(\theta_s)\mathbf{K} + (1 - \cos(\theta_s))\mathbf{K}^2)(\mathbf{x} - \mathbf{o}_r) + \mathbf{o}_r \quad (10)$$

where \mathbf{K} is a skew-symmetric matrix formed by the rotation axis \mathbf{a} and $\mathbf{I} \in \mathbb{R}^{3 \times 3}$ is a unit matrix. Meanwhile, we align the local quaternions of 3D Gaussian primitives after rotation through quaternion multiplication.

For the prismatic motion $m \cdot \mathbf{d} \in \mathbb{R}^3$, we take advantage of the vector space structure of Euclidean geometry by setting $s^* = 0$. The deformed position \mathbf{x}_s can be naturally acquired by linear interpolation without additional constraints, formulated as:

$$\mathbf{x}_s = \mathbf{x} + s \cdot m \cdot \mathbf{d} \quad (11)$$

unlike rotation motion, this parameterization avoids singularities due to the flat Riemannian structure of \mathbb{R}^3 .

However, the deformable fields should be applied exclusively to movable Gaussian primitives. Consequently, the Gaussian primitives need to be segmented into dynamic and

static parts. To address this challenge, we propose an unsupervised method for dynamic part segmentation. We first only input the multi-view images at the end state during warm-up training iterations, and then perform an initialization segmentation of the dynamic part. The segmentation criterion for the initial dynamic components is represented as: $|\Delta_{\mathbf{x}}| > \beta$, where $|\Delta_{\mathbf{x}}|$ is the L1 distance of spatial position variation during the warm-up training, and β is its average value. Furthermore, the spatial transformation of the dynamic part should align with the learnable motion parameters. Hence the dynamic part among the Gaussian primitives is re-evaluated at certain intervals of iterations, where the criterion for revolute or prismatic joints is represented as:

$$\begin{aligned} |\hat{\theta} - \theta| &< \frac{\varphi_{\theta}}{K} \\ |\hat{m} - m| &< \frac{\varphi_m}{K} \end{aligned} \quad (12)$$

where $\hat{\theta}$, \hat{m} are the rotation angle around axis \mathbf{a} and the translation distance respectively, φ is the tolerance threshold which decreases as the number of iterations K increases.

3.3. Optimization and Textured Mesh Extraction

Since the shapes of Gaussian primitives are not limited, the normal distributions of Gaussian primitives are difficult to estimate accurately. However, Gaussian’s normals should be parallel to the gradients of SDF in an ideal case. We consequently introduce additional regularization to regularize the normals of Gaussian primitives by SDF representation, expressed as follows:

$$\mathcal{L}_{normal} = \frac{1}{N} \sum_i^N \left(1 - \frac{|\mathbf{n}_i \cdot \nabla f(\mathbf{x}_i)|}{\|\mathbf{n}_i\| \cdot \|\nabla f(\mathbf{x}_i)\|}\right) \quad (13)$$

where \mathbf{n}_i represents the normal of Gaussian G_i , which is calculated following GOF:

$$\mathbf{n}_i = -R_i^T S_i^{-1} \mathbf{r}_L \quad (14)$$

where R is the rotation matrix encoded by Gaussian’s quaternion and S is the scaling matrix. We also employ the Eikonal regularization term [5] to encourage SDF gradient direction perpendicular to the surface, represented as:

$$\mathcal{L}_{eik} = \frac{1}{N} \sum_{i=1}^N (\|\nabla f(\mathbf{x}_i)\|_2 - 1)^2 \quad (15)$$

The overall training objective \mathcal{L} is formulated as follows:

$$\mathcal{L} = \mathcal{L}_c + \lambda_1 \mathcal{L}_{unbias} + \lambda_2 \mathcal{L}_{normal} + \lambda_3 \mathcal{L}_{eik} + \lambda_3 \mathcal{L}_d \quad (16)$$

where λ is the weight of regularization and \mathcal{L}_d is the depth distortion loss following [7]. \mathcal{L}_c is defined as:

$$\mathcal{L}_c = \lambda \mathcal{L}_{D-SSIM} + (1 - \lambda) \mathcal{L}_1 \quad (17)$$

where \mathcal{L}_{D-SSIM} is proposed in [11] and \mathcal{L}_1 is the L1 norm of the pixel loss.

Once the optimization converges, we adopt the TSDF fusion algorithm[22] to extract the textured mesh from Gaussian primitives. We utilize the α -blending rendering pipeline to obtain depth, opacity and RGB renderings for training views. Then we integrate these images into a voxel block grid (VBG) and extract a triangle mesh from the VBG. The textures of surface meshes can be efficiently obtained leveraging the spherical harmonics and opacity of Gaussian primitives. Please refer to our supplementary materials for a more detailed illustration.

4. Experiments

4.1. Experimental Setting

Datasets. We conduct surface reconstruction experiments on PartNet-Mobility [31] and AKB-48 [16] to evaluate the reconstruction quality of our method. The PartNet-Mobility dataset is a synthetic dataset comprising articulated objects across 46 categories, characterized by a diverse scale and geometry. Following PARIS, we selected the same 10 categories for our experiments. Each category comprises 64 to 100 RGB views at two arbitrary states, which are sampled randomly from their upper hemispheres. AKB-48 is a real-world dataset containing an extensive collection of articulated objects scanned in real indoor scenes. We select 5 categories with complicated geometry and texture and sample 100 RGB views as training inputs.

Metrics. Chamfer Distance (CD), F1-score and Earth Mover’s Distance (EMD) [40] are usually adopted as evaluation metrics for surface quality. However, these methods typically focus on the whole surface, endowing the unseen areas (such as the bottom of the object) with considerable weights during evaluation. This is unreasonable since we tend to be more concerned with the upper hemisphere regions of articulated objects. Therefore, we sample point clouds from the fragments between the rays cast by test cameras and the surface mesh to calculate EMD and Chamfer-L1 distance, defined as CD (rs). We also evaluate the F1-score and Chamfer-L1 distance for the whole surface, defined as CD (ws), to comprehensively evaluate the surface quality. Note that the CD values are multiplied by 1000 and the distance threshold of F1-score is set to 0.4. The calculation of these metrics can be referred to in our supplementary materials.

All the experiments are conducted on a single RTX 4090 GPU. We also provide detailed implementation of our approach and baselines in the supplementary materials.

4.2. Mesh Reconstruction Performance

We report the quantitative results of mesh reconstruction in Table. 1. As can be observed, our REArtGS outperforms

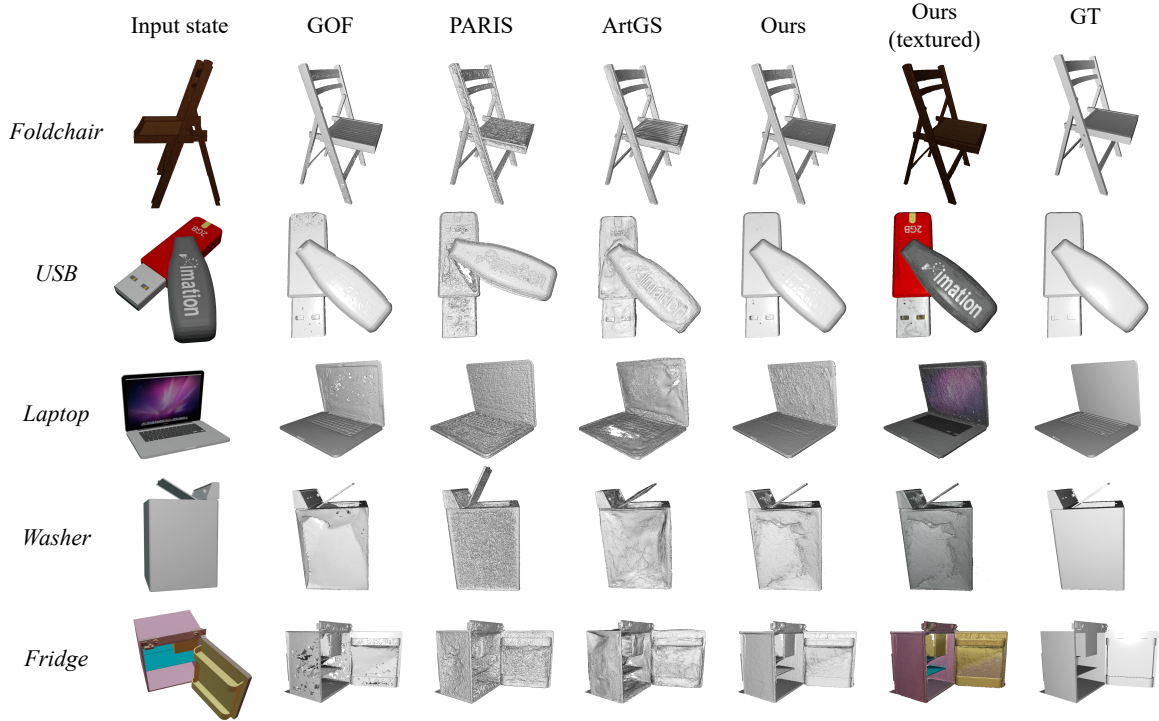


Figure 4. The qualitative result of surface reconstruction on PartNet-Mobility dataset. We show both textured and non-textured meshes for best comparison.

Metrics	Method	Stapler	USB	Scissor	Fridge	Foldchair	Washer	Blade	Laptop	Oven	Storage	Mean
CD(ws) ↓	A-SDF [21]	14.19	7.14	10.61	13.71	40.85	12.50	3.31	2.11	21.37	22.57	14.84
	Ditto [10]	2.38	2.09	1.70	2.16	6.80	7.29	42.04	<u>0.31</u>	2.51	3.91	7.19
	PARIS [15]	0.96	<u>1.80</u>	<u>0.30</u>	2.68	0.42	18.31	0.46	0.25	<u>6.07</u>	<u>8.12</u>	<u>3.94</u>
	GOF [39]	<u>1.51</u>	8.09	0.36	<u>1.51</u>	0.53	17.35	0.89	0.84	19.81	10.04	6.09
	ArtGS* [18]	2.77	1.36	0.75	2.01	<u>0.41</u>	20.59	<u>0.63</u>	0.99	9.01	9.00	4.75
	REArtGS (Ours)	3.47	0.75	0.29	1.50	0.40	<u>12.20</u>	0.72	0.53	8.89	8.27	3.79
CD(rs) ↓	A-SDF [23]	<u>2.140</u>	2.478	1.805	1.801	2.080	1.590	5.630	2.418	2.751	4.077	2.677
	Ditto [10]	2.874	3.049	2.926	1.550	0.925	<u>1.428</u>	5.792	1.184	1.296	2.837	2.386
	PARIS [15]	2.077	3.812	2.807	0.370	1.209	3.869	2.855	1.025	2.873	2.903	2.380
	GOF [39]	2.510	1.736	2.304	2.230	2.787	5.725	<u>2.111</u>	<u>0.961</u>	3.080	2.812	2.626
	ArtGS* [18]	2.949	<u>1.704</u>	2.438	0.725	<u>0.615</u>	2.874	2.031	1.182	<u>1.148</u>	1.157	<u>1.682</u>
	REArtGS (Ours)	2.186	1.433	<u>2.291</u>	<u>0.475</u>	0.018	1.204	2.596	0.038	0.784	<u>1.330</u>	1.236
F1 ↑	A-SDF [23]	0.041	0.035	0.094	0.019	0.053	0.046	0.224	0.001	0.010	0.015	0.054
	Ditto [10]	0.197	0.181	0.275	0.114	0.352	0.059	0.107	0.366	0.052	0.030	0.173
	PARIS [15]	0.240	0.151	0.343	0.091	0.429	0.024	0.396	0.533	0.031	0.033	0.227
	GOF [39]	0.217	0.189	0.614	0.173	<u>0.480</u>	0.087	0.386	0.303	0.049	0.036	<u>0.253</u>
	ArtGS* [18]	<u>0.251</u>	<u>0.209</u>	0.438	0.118	0.447	0.053	<u>0.408</u>	0.294	<u>0.056</u>	<u>0.042</u>	0.232
	REArtGS (Ours)	0.256	0.307	<u>0.598</u>	<u>0.165</u>	0.502	<u>0.069</u>	0.488	<u>0.419</u>	0.065	0.066	0.294
EMD ↓	A-SDF [23]	0.755	1.113	0.952	0.945	1.020	0.982	1.763	1.039	1.174	1.258	1.100
	Ditto [10]	1.724	1.308	1.212	0.619	0.935	<u>0.841</u>	1.996	0.417	<u>0.852</u>	0.970	1.087
	PARIS [15]	1.197	1.381	0.637	0.426	0.778	1.660	1.823	0.706	1.200	1.046	1.085
	GOF [39]	1.643	1.815	1.075	1.055	1.181	1.692	1.237	<u>0.394</u>	1.241	0.959	1.229
	ArtGS* [18]	1.921	0.677	<u>0.934</u>	0.637	<u>0.506</u>	1.154	<u>1.131</u>	0.502	1.006	<u>0.787</u>	<u>0.926</u>
	REArtGS (Ours)	<u>1.060</u>	<u>0.847</u>	1.078	<u>0.485</u>	0.097	0.777	1.112	0.111	0.627	0.755	0.695

Table 1. Quantitative results for the surface reconstruction quality on PartNet-Mobility dataset. We bold the best results and underline the second best results. * means we implement it without depth supervision for fair comparison.

state-of-the-art approaches in the mean across all metrics with **3.79**, **1.236**, **0.294** and **0.695** respectively. Compared to A-SDF [21] and Ditto [10] that exploits 3D inputs for ar-

ticulated object surface reconstruction, our method achieves higher reconstruction quality in the majority of categories. Although ditto surpasses our approach in several categories

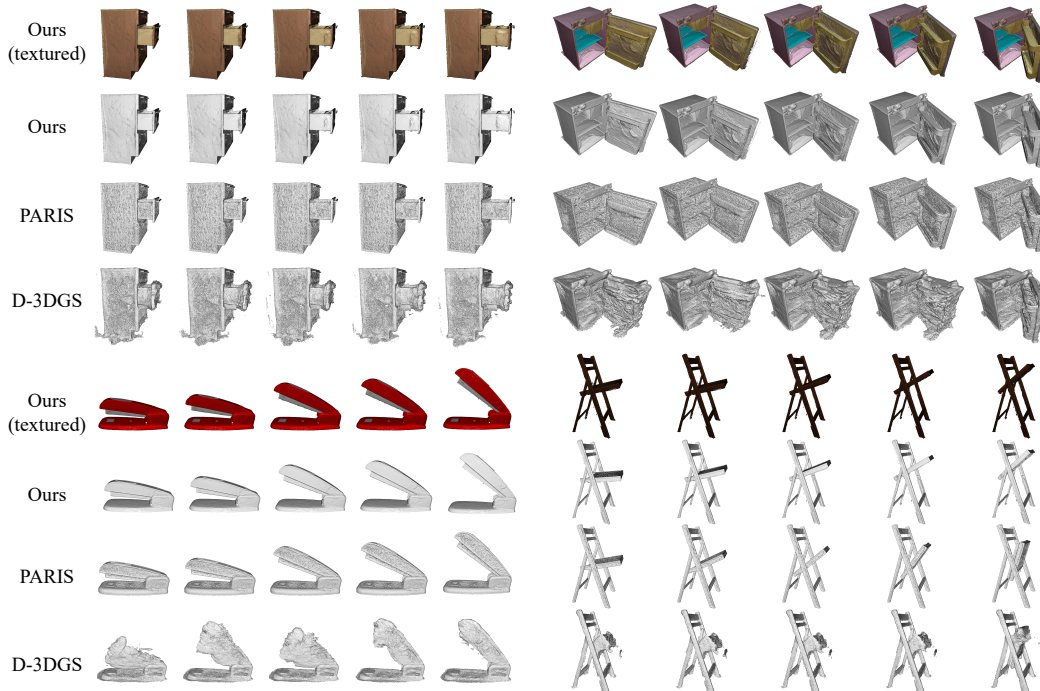


Figure 5. The qualitative results of surface generation at arbitrary unseen states on PartNet-Mobility dataset. We show both textured and non-textured meshes for best comparison. The states are sampled randomly.

Metrics	Method	Stapler	USB	Scissor	Fridge	Foldchair	Washer	Blade	Laptop	Oven	Storage	Mean
CD(ws) ↓	A-SDF [21]	112.30	34.01	94.11	33.46	56.73	55.82	3.78	27.64	29.60	25.30	47.28
	PARIS [15]	2.09	14.51	12.81	2.64	10.42	<u>18.30</u>	0.80	<u>3.25</u>	10.89	5.89	8.16
	D-3DGS [35]	98.90	16.79	91.84	48.78	30.10	30.93	1.262	65.11	22.39	18.79	42.49
	ArtGS* [18]	<u>2.34</u>	<u>1.72</u>	<u>0.68</u>	2.05	<u>0.52</u>	20.59	<u>0.63</u>	1.00	8.78	10.97	4.92
	REArtGS (Ours)	2.60	1.68	0.44	<u>2.21</u>	0.41	14.80	0.59	3.65	8.11	<u>6.48</u>	4.10
CD(rs) ↓	A-SDF [21]	8.992	1.806	1.822	5.166	5.668	7.050	5.991	2.710	5.245	7.794	5.224
	PARIS [15]	2.113	0.417	4.704	0.408	1.216	0.857	4.442	1.354	<u>2.793</u>	4.332	2.264
	D-3DGS [35]	9.589	1.544	0.891	0.465	<u>1.147</u>	3.218	0.168	<u>0.449</u>	3.773	3.100	2.434
	ArtGS* [18]	4.924	0.670	<u>0.381</u>	0.471	1.622	2.670	1.455	1.269	3.912	0.562	<u>1.794</u>
	REArtGS (Ours)	<u>3.651</u>	<u>0.487</u>	0.127	<u>0.464</u>	0.420	<u>1.617</u>	<u>0.414</u>	0.298	2.129	<u>1.020</u>	1.063
F1 ↑	A-SDF [21]	0.007	0.034	0.056	0.012	0.021	0.023	0.168	0.001	0.010	0.004	0.034
	PARIS [15]	0.221	0.151	0.319	0.091	0.423	0.024	0.421	<u>0.530</u>	0.031	0.032	0.224
	D-3DGS [35]	0.064	0.180	0.125	0.073	0.168	0.195	0.233	0.131	0.022	0.023	0.121
	ArtGS* [18]	0.264	0.255	<u>0.454</u>	<u>0.125</u>	<u>0.460</u>	<u>0.055</u>	<u>0.426</u>	0.292	<u>0.062</u>	<u>0.045</u>	<u>0.244</u>
	REArtGS (Ours)	<u>0.254</u>	<u>0.215</u>	0.577	0.186	0.465	0.052	0.509	0.608	0.065	0.050	0.298
EMD ↓	A-SDF [21]	<u>2.123</u>	0.951	0.955	1.606	1.684	1.878	1.731	1.115	1.620	1.837	1.559
	PARIS [15]	2.454	0.457	1.533	0.451	0.780	0.655	1.491	0.770	<u>1.183</u>	1.354	1.113
	D-3DGS [35]	3.224	0.612	0.665	0.481	0.758	1.269	0.291	<u>0.436</u>	1.374	1.206	1.032
	ArtGS* [18]	2.207	0.562	<u>0.412</u>	0.563	<u>0.525</u>	1.171	0.631	0.724	1.297	<u>0.750</u>	<u>0.884</u>
	REArtGS (Ours)	1.594	<u>0.494</u>	0.251	<u>0.473</u>	0.459	<u>0.900</u>	<u>0.456</u>	0.353	1.033	0.689	0.670

Table 2. Quantitative results for the surface generation quality on PartNet-Mobility dataset. We bold the best results and underline the second best results. * means we implement it without depth supervision for fair comparison.

(Washer, Oven, and Storage), it employs additional 3D data for pre-training and requires the united robotics description format (URDF) files of articulated objects. However, our method merely requires the RGB view collections at two arbitrary states, which is more convenient in practical applications. In terms of PARIS that utilizes the neural implicit representation for surface reconstruction, our approach ex-

hibits significantly smoother and clearer surfaces, as shown in Fig. 4. Although PARIS slightly outperforms our approach in a few categories of CD (ws), it exhibits considerable disadvantages compared with our approach in CD (rs) and EMD scores, which better evaluate the substantial surface quality. As for the 3DGS-based reconstruction method GOF, our approach achieves marked superiority in the vast

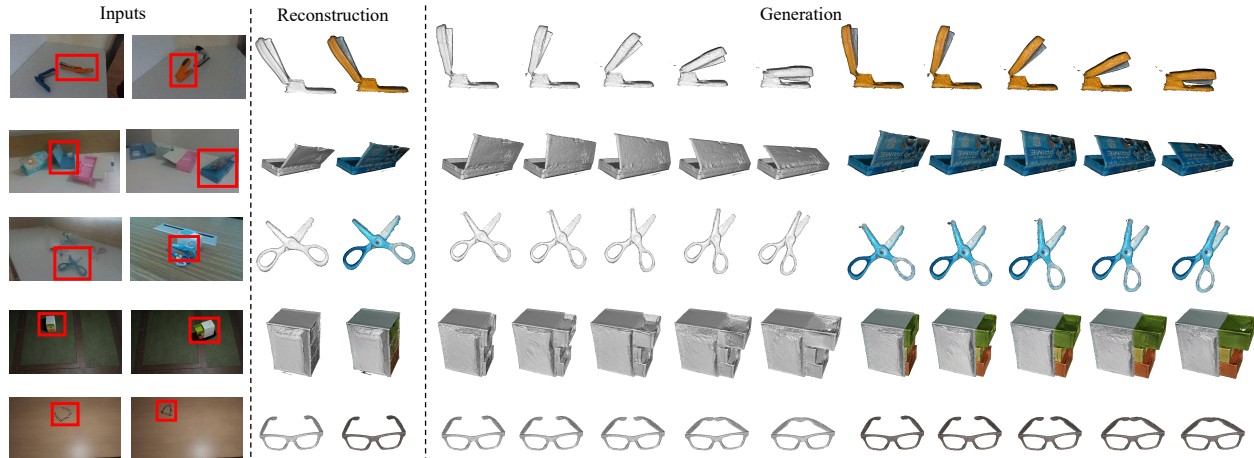


Figure 6. The qualitative results of surface reconstruction on real-world AKB-48 [16] repository. The multi-view images are obtained from ReArtVal [17] dataset. We show both textured and non-textured meshes for best view.

majority of categories. This is primarily attributed to our geometric constraints regularizing the opacity fields and facilitating more reasonable distribution of 3D Gaussian primitives over scene surfaces.

4.3. Mesh Generation Performance

We report the quantitative results of mesh reconstruction in Table. 2 and present the qualitative results Fig. 5. Please refer to our supplementary material for more qualitative results. Our REArtGS achieves the best mean results across all metrics with **4.10**, **1.063**, **0.298** and **0.670**. Compared to PARIS, our method exhibits smoother surface generation results, as shown in Fig. 5. It is mainly because PARIS lacks a reasonable geometry initiation and directly utilizes the composite rendering, leading to the spatial overlap between the neural radiation fields of the start and end states. In contrast, our approach utilizes the accurate dense points from the reconstruction stage and optimizes the deformable fields to yield dynamic results, maintaining high-quality surface during generation.

It can be observed that our method is significantly superior to D-3DGS on most categories. As presented in Fig. 5, D-3DGS fails to accurately generate the surface of unseen states only using merely two states of RGB supervision. This is attributed to the fact that its deformation fields are exclusively derived from MLP. In contrast, our method accurately recovers the unseen states through the motion constraints.

4.4. Ablation Studies

We conduct an ablation of the unbiased SDF guidance on PartNet-Mobility dataset to validate its effectiveness. The ablation setting and results are reported in Table. 3. The quantitative results prove that both SDF guidance and the unbiased regularization of SDF indeed improve surface reconstruction quality. This is primarily because the SDF

representation establishes explicit geometric association between the opacity fields and scene surface through Φ_k , and the unbiased SDF regularization further optimizes the distribution of Gaussian opacity fields.

w/ SDF	w/ Unbiased Reg.	CD (ws)	CD (rs)	F1	EMD
		5.96	2.242	0.250	1.366
✓		4.38	1.921	0.273	0.817
✓	✓	3.79	1.236	0.294	0.695

Table 3. The ablation study of the unbiased SDF guidance on PartNet-Mobility dataset.

We also conduct an ablation study of the motion constraints on PartNet-Mobility dataset and present the quantitative results in Table. 4. For the baseline without motion constraints, we employ three MLPs to learn the variations of spatial positions, scales, and quaternions respectively for Gaussian primitives, which is similar to D-3DGS. The significantly superior results demonstrate the effectiveness of the motion constraints. Actually, motion constraints effectively compress the parameter search space of the deformation fields according to the kinematic structures of articulated objects and accurately infer the deformed spatial positions via rigid transformation.

Settings	CD (ws)	CD (rs)	F1	EMD
w/o motion constraints	18.65	2.270	0.209	1.105
w/ motion constraints	5.41	1.063	0.276	0.670

Table 4. The ablation study of motion constraints. We compare the surface generation quality on the PartNet-Mobility dataset between training with motion constraints and without motion constraints.

4.5. Generalization to the Real World

We conduct reconstruction and generation experiments in the real world to investigate the generalization capacity of our REArtGS. We report the quantitative results comparing

with PARIS in Table. 5, and present the qualitative results in Fig. 6. Our approach significantly outperforms PARIS in mean performance across all metrics. This demonstrates that our method exhibits strong generalization capability for real-world objects and enables high-quality surface reconstruction and generation as shown in Fig. 6.

Category	Method	Reconstruction				Generation			
		CD(ws)↓	CD(rs)↓	F1↑	EMD↓	CD(ws)↓	CD(rs)↓	F1↑	EMD↓
Box	PARIS [15]	<u>4.69</u>	1.651	0.097	0.843	<u>3.98</u>	2.131	0.306	1.055
	ArtGS* [18]	8.61	<u>0.967</u>	<u>0.143</u>	<u>0.697</u>	10.23	<u>1.606</u>	<u>0.309</u>	<u>0.851</u>
	REArtGS (Ours)	2.49	0.898	0.205	0.671	1.28	1.425	0.559	0.845
Stapler	PARIS [15]	0.23	0.104	0.551	0.165	0.47	0.198	0.540	0.194
	ArtGS* [18]	51.04	1.364	0.476	0.827	5.13	0.527	0.533	0.514
	REArtGS (Ours)	<u>0.24</u>	0.037	0.728	0.137	0.34	0.044	0.582	0.151
Scissor	PARIS [15]	<u>0.18</u>	0.302	<u>0.710</u>	0.314	<u>0.18</u>	0.329	0.424	0.310
	ArtGS* [18]	11.43	<u>0.073</u>	0.588	<u>0.192</u>	5.53	<u>0.089</u>	<u>0.600</u>	<u>0.213</u>
	REArtGS (Ours)	0.08	0.017	0.902	0.093	0.08	0.003	0.899	0.042
Cutter	PARIS [15]	<u>2.56</u>	1.371	0.570	<u>0.302</u>	45.02	1.684	0.309	1.183
	ArtGS* [18]	5.65	<u>0.453</u>	<u>0.644</u>	0.477	65.64	1.298	0.093	0.806
	REArtGS (Ours)	0.13	0.016	0.874	0.090	<u>51.56</u>	<u>1.559</u>	<u>0.228</u>	<u>0.884</u>
Drawer	PARIS [15]	30.63	4.568	0.062	<u>1.577</u>	33.94	3.865	0.091	1.430
	ArtGS* [18]	19.41	7.478	0.086	1.935	12.60	1.624	<u>0.094</u>	0.911
	REArtGS (Ours)	10.73	2.607	0.138	1.142	11.71	<u>1.739</u>	0.209	<u>0.933</u>
Eyeglasses	PARIS [15]	<u>0.16</u>	1.582	<u>0.637</u>	0.212	<u>0.18</u>	1.550	0.609	1.284
	ArtGS* [18]	27.49	<u>1.384</u>	0.557	<u>0.832</u>	12.12	1.592	<u>0.747</u>	<u>0.955</u>
	REArtGS (Ours)	0.04	0.018	0.969	0.096	0.04	<u>1.568</u>	0.974	0.886
Mean	PARIS [15]	<u>6.41</u>	1.336	0.438	<u>0.569</u>	13.96	1.626	0.380	0.707
	ArtGS* [18]	20.61	1.953	0.416	0.826	18.54	<u>1.123</u>	<u>0.396</u>	0.708
	REArtGS (Ours)	2.86	0.599	0.636	0.372	10.83	1.056	0.575	0.624

Table 5. The quantitative results on real-world AKB-48 dataset. We bold the best results and underline the second best results. * means we implement it without depth supervision for fair comparison.

5. Conclusion and Future Work

We propose REArtGS, a novel framework that achieves high-quality textured mesh reconstruction and dynamic generation of articulated objects using only RGB views of two arbitrary states. We propose an unbiased SDF guidance to regularize Gaussian opacity fields and model the Gaussian deformation fields constrained by kinematic structures for generating meshes of unseen states. Experiments show the superior performance of our method on both synthetic and real-world data.

The limitations of REArtGS lie on the requirement of camera pose prior and challenges of objects with transparent materials. Future works will introduce relative pose estimation to alleviate the dependence on camera poses and employ physically-based networks to model the transparent materials.

References

- [1] Danpeng Chen, Hai Li, Weicai Ye, Yifan Wang, Weijian Xie, Shangjin Zhai, Nan Wang, Haomin Liu, Hujun Bao, and Guofeng Zhang. Pgsr: Planar-based gaussian splatting for efficient and high-fidelity surface reconstruction. *IEEE Transactions on Visualization and Computer Graphics*, 2024. 1, 2
- [2] Hanlin Chen, Chen Li, and Gim Hee Lee. Neusg: Neural implicit surface reconstruction with 3d gaussian splatting guidance. *arXiv preprint arXiv:2312.00846*, 2023. 2
- [3] Pinxuan Dai, Jiamin Xu, Wenxiang Xie, Xinguo Liu, Huamin Wang, and Weiwei Xu. High-quality surface reconstruction using gaussian surfels. In *ACM SIGGRAPH 2024 Conference Papers*, pages 1–11, 2024. 2
- [4] Yuanxing Duan, Fangyin Wei, Qiyu Dai, Yuhang He, Wenzheng Chen, and Baoquan Chen. 4d gaussian splatting: Towards efficient novel view synthesis for dynamic scenes. *arXiv e-prints*, pages arXiv–2402, 2024. 2
- [5] Amos Gropp, Lior Yariv, Niv Haim, Matan Atzmon, and Yaron Lipman. Implicit geometric regularization for learning shapes. *arXiv preprint arXiv:2002.10099*, 2020. 5
- [6] Antoine Guédon and Vincent Lepetit. Sugar: Surface-aligned gaussian splatting for efficient 3d mesh reconstruction and high-quality mesh rendering. In *Proceedings of the IEEE/CVF Conference on Computer Vision and Pattern Recognition*, pages 5354–5363, 2024. 2
- [7] Binbin Huang, Zehao Yu, Anpei Chen, Andreas Geiger, and Shenghua Gao. 2d gaussian splatting for geometrically accurate radiance fields. In *ACM SIGGRAPH 2024 conference papers*, pages 1–11, 2024. 1, 2, 5
- [8] Muhammad Zubair Irshad, Thomas Kollar, Michael Laskey, Kevin Stone, and Zsolt Kira. Centersnap: Single-shot multi-object 3d shape reconstruction and categorical 6d pose and size estimation. In *2022 International Conference on Robotics and Automation (ICRA)*, pages 10632–10640. IEEE, 2022. 2
- [9] Muhammad Zubair Irshad, Sergey Zakharov, Rares Ambrus, Thomas Kollar, Zsolt Kira, and Adrien Gaidon. Shapo: Implicit representations for multi-object shape, appearance, and pose optimization. In *European Conference on Computer Vision*, pages 275–292. Springer, 2022. 2
- [10] Zhenyu Jiang, Cheng-Chun Hsu, and Yuke Zhu. Ditto: Building digital twins of articulated objects from interaction. In *Proceedings of the IEEE/CVF Conference on Computer Vision and Pattern Recognition*, pages 5616–5626, 2022. 2, 6
- [11] Bernhard Kerbl, Georgios Kopanas, Thomas Leimkühler, and George Drettakis. 3d gaussian splatting for real-time radiance field rendering. *ACM Trans. Graph.*, 42(4):139–1, 2023. 1, 2, 5
- [12] Jiyang Li, Lechao Cheng, Zhangye Wang, Tingting Mu, and Jingxuan He. Loopgaussian: creating 3d cinemagraph with multi-view images via eulerian motion field. In *Proceedings of the 32nd ACM International Conference on Multimedia*, pages 476–485, 2024. 2
- [13] Kailin Li, Jingbo Wang, Lixin Yang, Cewu Lu, and Bo Dai. Semgrasp: Semantic grasp generation via language aligned discretization. In *European Conference on Computer Vision*, pages 109–127. Springer, 2024. 1
- [14] Isabella Liu, Hao Su, and Xiaolong Wang. Dynamic gaussians mesh: Consistent mesh reconstruction from monocular videos. *arXiv preprint arXiv:2404.12379*, 2024. 2
- [15] Jiayi Liu, Ali Mahdavi-Amiri, and Manolis Savva. Paris: Part-level reconstruction and motion analysis for articulated objects. In *Proceedings of the IEEE/CVF International Conference on Computer Vision*, pages 352–363, 2023. 1, 2, 6, 7, 9

- [16] Liu Liu, Wenqiang Xu, Haoyuan Fu, Sucheng Qian, Qiaojun Yu, Yang Han, and Cewu Lu. Akb-48: A real-world articulated object knowledge base. In *Proceedings of the IEEE/CVF Conference on Computer Vision and Pattern Recognition*, pages 14809–14818, 2022. 2, 5, 8
- [17] Liu Liu, Han Xue, Wenqiang Xu, Haoyuan Fu, and Cewu Lu. Toward real-world category-level articulation pose estimation. *IEEE Transactions on Image Processing*, 31:1072–1083, 2022. 1, 8
- [18] Yu Liu, Baoxiong Jia, Ruijie Lu, Junfeng Ni, Song-Chun Zhu, and Siyuan Huang. Building interactable replicas of complex articulated objects via gaussian splatting. In *The Thirteenth International Conference on Learning Representations*, 2025. 6, 7, 9
- [19] Lars Mescheder, Michael Oechsle, Michael Niemeyer, Sebastian Nowozin, and Andreas Geiger. Occupancy networks: Learning 3d reconstruction in function space. In *Proceedings of the IEEE/CVF conference on computer vision and pattern recognition*, pages 4460–4470, 2019. 2
- [20] Ben Mildenhall, Pratul P Srinivasan, Matthew Tancik, Jonathan T Barron, Ravi Ramamoorthi, and Ren Ng. Nerf: Representing scenes as neural radiance fields for view synthesis. *Communications of the ACM*, 65(1):99–106, 2021. 2
- [21] Jiteng Mu, Weichao Qiu, Adam Kortylewski, Alan Yuille, Nuno Vasconcelos, and Xiaolong Wang. A-sdf: Learning disentangled signed distance functions for articulated shape representation. In *Proceedings of the IEEE/CVF International Conference on Computer Vision*, pages 13001–13011, 2021. 2, 6, 7
- [22] Richard A Newcombe, Shahram Izadi, Otmar Hilliges, David Molyneaux, David Kim, Andrew J Davison, Pushmeet Kohi, Jamie Shotton, Steve Hodges, and Andrew Fitzgibbon. Kinectfusion: Real-time dense surface mapping and tracking. In *2011 10th IEEE international symposium on mixed and augmented reality*, pages 127–136. Ieee, 2011. 5
- [23] Jeong Joon Park, Peter Florence, Julian Straub, Richard Newcombe, and Steven Lovegrove. DeepSDF: Learning continuous signed distance functions for shape representation. In *Proceedings of the IEEE/CVF conference on computer vision and pattern recognition*, pages 165–174, 2019. 2, 6
- [24] E Piña. Rotations with rodrigues’ vector. *European journal of physics*, 32(5):1171, 2011. 4
- [25] Minghan Qin, Wanhua Li, Jiawei Zhou, Haoqian Wang, and Hanspeter Pfister. Langsplat: 3d language gaussian splatting. In *Proceedings of the IEEE/CVF Conference on Computer Vision and Pattern Recognition*, pages 20051–20060, 2024. 2
- [26] Marie-Julie Rakotosaona, Fabian Manhardt, Diego Martin Arroyo, Michael Niemeyer, Abhijit Kundu, and Federico Tombari. Nerfmeshing: Distilling neural radiance fields into geometrically-accurate 3d meshes. In *2024 international conference on 3D vision (3DV)*, pages 1156–1165. IEEE, 2024. 2
- [27] Chaoyue Song, Jiacheng Wei, Chuan Sheng Foo, Guosheng Lin, and Fayao Liu. Reacto: Reconstructing articulated objects from a single video. In *Proceedings of the IEEE/CVF Conference on Computer Vision and Pattern Recognition*, pages 5384–5395, 2024. 2
- [28] Jiayang Tang, Hang Zhou, Xiaokang Chen, Tianshu Hu, Errui Ding, Jingdong Wang, and Gang Zeng. Delicate textured mesh recovery from nerf via adaptive surface refinement. In *Proceedings of the IEEE/CVF International Conference on Computer Vision*, pages 17739–17749, 2023. 2
- [29] Junbo Wang, Wenhai Liu, Qiaojun Yu, Yang You, Liu Liu, Weiming Wang, and Cewu Lu. Rpmart: Towards robust perception and manipulation for articulated objects. In *2024 IEEE/RSJ International Conference on Intelligent Robots and Systems (IROS)*, pages 7270–7277. IEEE, 2024. 1
- [30] Peng Wang, Lingjie Liu, Yuan Liu, Christian Theobalt, Taku Komura, and Wenping Wang. Neus: Learning neural implicit surfaces by volume rendering for multi-view reconstruction. *arXiv preprint arXiv:2106.10689*, 2021. 3
- [31] Fanbo Xiang, Yuzhe Qin, Kaichun Mo, Yikuan Xia, Hao Zhu, Fangchen Liu, Minghua Liu, Hanxiao Jiang, Yifu Yuan, He Wang, et al. Sapien: A simulated part-based interactive environment. In *Proceedings of the IEEE/CVF conference on computer vision and pattern recognition*, pages 11097–11107, 2020. 2, 5
- [32] Haodong Xiang, Xinghui Li, Xiansong Lai, Wanting Zhang, Zhichao Liao, Kai Cheng, and Xueping Liu. Gaussian-room: Improving 3d gaussian splatting with sdf guidance and monocular cues for indoor scene reconstruction. *arXiv preprint arXiv:2405.19671*, 2024. 2
- [33] Han Xue, Liu Liu, Wenqiang Xu, Haoyuan Fu, and Cewu Lu. Omad: Object model with articulated deformations for pose estimation and retrieval. 2021. 1
- [34] Lixin Yang, Kailin Li, Xinyu Zhan, Fei Wu, Anran Xu, Liu Liu, and Cewu Lu. Oakink: A large-scale knowledge repository for understanding hand-object interaction. In *Proceedings of the IEEE/CVF conference on computer vision and pattern recognition*, pages 20953–20962, 2022. 1
- [35] Ziyi Yang, Xinyu Gao, Wen Zhou, Shaohui Jiao, Yuqing Zhang, and Xiaogang Jin. Deformable 3d gaussians for high-fidelity monocular dynamic scene reconstruction. In *Proceedings of the IEEE/CVF conference on computer vision and pattern recognition*, pages 20331–20341, 2024. 2, 7
- [36] Mulin Yu, Tao Lu, Linning Xu, Lihan Jiang, Yuanbo Xiangli, and Bo Dai. Gsdg: 3dgs meets sdf for improved rendering and reconstruction. *arXiv preprint arXiv:2403.16964*, 2024. 2
- [37] Qiaojun Yu, Junbo Wang, Wenhai Liu, Ce Hao, Liu Liu, Lin Shao, Weiming Wang, and Cewu Lu. Gamma: Generalizable articulation modeling and manipulation for articulated objects. In *2024 IEEE International Conference on Robotics and Automation (ICRA)*, pages 5419–5426. IEEE, 2024. 1
- [38] Zehao Yu, Anpei Chen, Binbin Huang, Torsten Sattler, and Andreas Geiger. Mip-splatting: Alias-free 3d gaussian splatting. In *Proceedings of the IEEE/CVF conference on computer vision and pattern recognition*, pages 19447–19456, 2024. 2
- [39] Zehao Yu, Torsten Sattler, and Andreas Geiger. Gaussian opacity fields: Efficient adaptive surface reconstruction in unbounded scenes. *ACM Transactions on Graphics (TOG)*, 43(6):1–13, 2024. 1, 2, 6

- [40] Chi Zhang, Yujun Cai, Guosheng Lin, and Chunhua Shen. Deepemd: Differentiable earth mover's distance for few-shot learning. *IEEE Transactions on Pattern Analysis and Machine Intelligence*, 45(5):5632–5648, 2022. [5](#)